

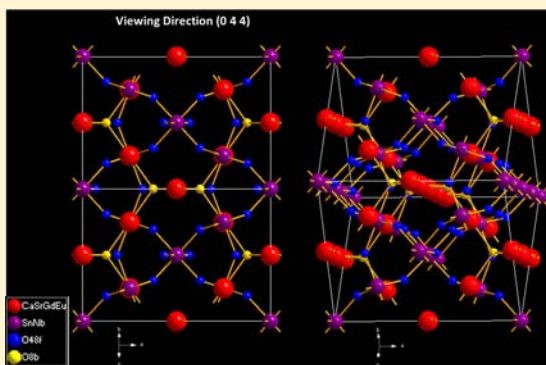
Influence of Cation Substitution and Activator Site Exchange on the Photoluminescence Properties of Eu^{3+} -Doped Quaternary Pyrochlore Oxides

S. K. Mahesh, P. Prabhakar Rao,* Mariyam Thomas, T. Linda Francis, and Peter Koshy

Materials Science and Technology Division, National Institute for Interdisciplinary Science and Technology (NIIST), CSIR, Trivandrum 695 019, India

Supporting Information

ABSTRACT: Stannate-based pyrochlore-type red phosphors $\text{CaGd}_{1-x}\text{SnNbO}_7:x\text{Eu}^{3+}$, $\text{Ca}_{1-y}\text{Sr}_y\text{Gd}_{1-x}\text{SnNbO}_7:x\text{Eu}^{3+}$, and $\text{Ca}_{0.8-x}\text{Sr}_{0.2}\text{GdSnNbO}_{7+\delta}:x\text{Eu}^{3+}$ were prepared via conventional solid-state method. Influence of cation substitution and activator site control on the photoluminescence properties of these phosphors are elucidated using powder X-ray diffraction, Rietveld analysis, Raman spectrum analysis, and photoluminescence excitation and emission spectra. The Eu^{3+} luminescence in quaternary pyrochlore lattice exemplifies as a very good structural probe for the detection of short-range disorder in the lattice, which otherwise is not detected by normal powder X-ray diffraction technique. The Eu^{3+} emission due to magnetic dipole transition ($^5\text{D}_0\text{--}^7\text{F}_1$ MD) is modified with the increase in europium concentration in the quaternary pyrochlore red phosphors. $^5\text{D}_0\text{--}^7\text{F}_1$ MD transition splitting is not observable for low Eu^{3+} doping because of the short-range disorder in the pyrochlore lattice. Appearance of narrow peaks in Raman spectra confirms that short-range disorder in the crystal lattice disappears with progressive europium doping. By using Sr as a network modifier ion in place of Ca we were able to increase the f–f transition intensities and europium quenching concentration. The influence of effective positive charge of the central Eu^{3+} ions when it replaces a metal ion having lower oxidation state such as Ca^{2+} was also investigated. The relative intensities of A_{1g} ($\sim 500\text{ cm}^{-1}$) and F_{2g} ($\sim 330\text{ cm}^{-1}$) Raman vibrational modes get inverted when Eu^{3+} ions replaces Ca^{2+} ions instead of Gd^{3+} as trivalent europium ions can attract the electron cloud of oxygen ions strongly in comparison with divalent calcium ions. The influence of positive charge effect of Eu^{3+} in $\text{Ca}_{0.7}\text{Sr}_{0.2}\text{GdSnNbO}_{7+\delta}:0.1\text{Eu}^{3+}$ phosphor is greatly strengthened the charge transfer band and $^7\text{F}_0\text{--}^5\text{L}_6$ transition intensities than that of the $\text{Ca}_{0.8}\text{Sr}_{0.2}\text{Gd}_{0.9}\text{SnNbO}_7:0.1\text{Eu}^{3+}$ phosphor. Our results suggest that the photoluminescence properties can be enhanced by simple compositional adjustments in the quaternary pyrochlore-type red phosphors.



1. INTRODUCTION

Among the rare-earth-doped phosphors, Eu^{3+} luminescence has attained great importance because of its simple electronic energy level scheme and the hypersensitive transitions that can be used as a probe for site symmetry studies,^{1,2} structure–luminescence correlations,^{3,4} covalency/polarizability effect of ligands,⁵ chemical bond differences in solids,⁶ etc. Eu^{3+} emission spectra consist of a series of sharp lines arising from intraconfigurational $^5\text{D}_0\text{--}^7\text{F}_j$ transitions in which $^5\text{D}_0\text{--}^7\text{F}_1$ magnetic dipole (MD) transition around 590 nm or $^5\text{D}_0\text{--}^7\text{F}_2$ electric dipole (ED) transition around 612 nm dominates depending on the site symmetry of Eu^{3+} sites. When Eu^{3+} locates in a site with inversion symmetry MD transitions dominates otherwise the ED transition.⁷ Splitting of these transitions give an insight into the crystal field effect at the activator sites.^{8,9} The appearance of $^5\text{D}_0\text{--}^7\text{F}_0$ transition of Eu^{3+} is an indication of lowering of Eu^{3+} crystal site symmetry as it is allowed only for C_2 , C_m , C_{nv} site symmetries and it shows a red shift with the increase in covalency of Eu^{3+} .^{1,10} Eu^{3+} -doped phosphor materials that can be excited in the vacuum

ultraviolet region found applications in the field of plasma display panels, field-emission displays, high-pressure Hg discharge lamps, etc.¹¹ But, highly efficient, low-power-consuming, solid-state lighting technology requires phosphors that are excitable under near UV ($\sim 395\text{ nm}$) or blue light ($\sim 465\text{ nm}$). Eu^{3+} -doped red phosphors attained much attention in the area of phosphor converted white-light-emitting diodes because they exhibit a high lumen equivalent, quantum efficiency, and photostability at the same time.¹²

Pyrochlore compounds with a general formula $\text{A}_2\text{B}_2\text{O}_7$ offer good qualities of a host lattice such as high chemical stability, lattice stiffness, thermal stability, etc., and at the same time allows a wide variety of chemical substitutions at the A and B sites (3^+ and 4^+ or 2^+ and 5^+ combinations of valence, as well as oxygen vacancies).¹³ The unit cell of this structure is usually face-centered cubic with a space group $Fd\bar{3}m$ with eight formula units per unit cell ($Z = 8$). The A site ($16d$) cation is in 8-fold

Received: March 7, 2013

Published: November 14, 2013

coordination with oxygen anions, whereas the smaller B site (16c) cation resides in 6-fold coordination forming a (BO₆) oxygen octahedra. Cations having higher ionic radii (~1 Å) occupy the A-site, and the lower one (~0.6 Å) goes to the B sites. In pyrochlore phosphors, Eu³⁺ (ionic radius 1.067 Å, CN8) is expected to occupy A-site having site symmetry D_{3d}. The inversion symmetry of the pyrochlore A site makes it difficult to get narrow red emission band through ED transition by Eu³⁺ doping. Though red emitting pyrochlore phosphors are reported,^{14–16} most of the Eu³⁺-doped pyrochlore phosphors give MD dominated orange emission.^{17–19} The oxygen has two distinct sites: oxygen ions on the 48f site, which are bonded tetrahedrally to two A and two B cations, and those on 8b sites (O') that are bonded tetrahedrally to four A cations (8a site is vacant in an ideal pyrochlore structure taking B as origin, this vacant 8a site is coordinated by four B cations). All the A and B cations and oxygen ions in the 8b sites are on special positions but the 48f oxygen position varies. The A and B site coordination polyhedra are joined along edges, and the shapes of these polyhedra change as the positional parameter 'x' of the O_{48f} shifts to accommodate cations of different sizes. These two polyhedra have D_{3d} symmetry. For x = 0.3750, the A site coordination polyhedron is a regular cube, and the B site polyhedron is distorted to a trigonally flattened octahedron. In this case, materials have a defect fluorite structure and occupancy of each anion site is 0.875. For x = 0.3125, the B site is a regular octahedron and the A site is a distorted scalenohedron, and materials have the ideal pyrochlore structure. Thus, the 48f oxygen positional parameter, x defines the polyhedral distortion and structural deviation from the ideal fluorite structure.

Yang et al. reported the Eu³⁺-doped luminescence properties of Gd₂Sn₂O₇ phosphors.²⁰ In the emission spectra of these phosphors, MD transition intensity dominates over ED transition because of the inversion symmetry of Eu³⁺ sites and the excitation spectra has weak f–f transition intensities in comparison with charge transfer (CT) band intensity. For an enhanced parity forbidden red emission in pyrochlore phosphors either we have to destruct the inversion symmetry of Eu³⁺ site or reduce the CT band energy such that there will be an enhanced probability of mixing of CT band wave function with f orbital and thereby a relaxation in the parity selection rule.⁷ Incorporation of cations with different valency and electronegativity to the crystal lattice can cause local distortion and modification in polarizability of chemical environment of Eu³⁺, which can change the photoluminescent properties.^{10,21–23} In the present study, we tried to enhance the f–f transition intensity of gadolinium stannate pyrochlore phosphors by incorporating Ca²⁺ ions to the A site and Nb⁵⁺ ions to the B site. Ordered pyrochlore compounds can have short-range disorder which is very difficult to detect from X-ray diffraction studies. Absence of ⁵D₀–⁷F₁ MD transition splitting for low europium doping concentration in CaGd_{1-x}SnNbO₇:xEu³⁺ gives some information about short-range disorder in the pyrochlore crystal lattice. The substitution of calcium ions by bigger strontium ions found to have influence on the concentration quenching. The influence of effective positive charge of the central Eu³⁺ ions when it replaces a metal ion having lower oxidation state is also a question of interest. Though it is reported that the effective positive charge of the central activator ion will shift the charge transfer band to lower energy region, its extent of influence on CT band and f–f excitation is very difficult to estimate because

of the absence of suitable host system.²⁴ The present quaternary pyrochlore CaGdSnNbO₇ offers such kind of studies as the Eu³⁺ ion can be doped to Ca²⁺/Gd³⁺ ions without any significant change in the structure/electronegativity of ligands and it was found that doping of Eu³⁺ ions to the Ca²⁺ ion site leads to some drastic increase in the f–f excitation peaks and in emission intensity, which is somewhat interesting because in most cases, better luminescence properties are observed for isovalent substitution. The luminescence emission changes with respect to bigger cation substitution and aliovalent doping is also discussed in detail in this work.

2. EXPERIMENTAL SECTION

The pyrochlore compounds CaGd_{1-x}SnNbO₇:xEu³⁺, Ca_{1-y}Sr_yGd_{1-x}SnNbO₇:xEu³⁺ and Ca_{0.8-x}Sr_{0.2}GdSnNbO_{7+δ}:xEu³⁺ were synthesized through a solid state method using CaCO₃, SrCO₃, Gd₂O₃, Eu₂O₃, SnO₂, and Nb₂O₅. The precursors are from the M/s Across Organics with 99.9% purity and the precursor oxides are fine powders. These precursors were taken in the required stoichiometric ratios and mixed thoroughly in an agate mortar using acetone as a wetting medium until fine slurry was obtained. The slurry was dried by placing it in an air oven at a temperature of 100 °C. This process of mixing and drying was repeated thrice to get a homogeneous product. These products were calcined at 1300–1400 °C for 6 h with intermittent grinding until a phase-pure compound was obtained. The electrical heating of the furnace is programmed initially 10 °C/min up to 900 °C and then onward 5 °C/min until the desired temperature, 1300–1400 °C. The calcined product was then ground into a fine powder for carrying further characterizations. CaGd_{1-x}SnNbO₇:xEu³⁺ and Ca_{1-y}Sr_yGd_{1-x}SnNbO₇:xEu³⁺ compounds were calcined at 1300 °C for 6 h. Ca_{0.8-x}Sr_{0.2}GdSnNbO_{7+δ}:xEu³⁺ phosphors give better luminescence properties when calcined at 1300 and 1400 °C for 6 h.

X-ray powder diffraction (XRD) analysis was performed with a PANalytical X'Pert Pro diffractometer having Ni filtered Cu–Kα radiation with X-ray tube operating at 40 kV, 30 mA, and 2θ varied from 10 to 90° in 0.016° steps. Structure refinement of the XRD data was performed by Rietveld analysis using GSAS program.²⁵ The obtained powder data was refined using the starting model of Gd₂Sn₂O₇ with the origin placed on B site and the space group Fd $\bar{3}m$ (No. 227) of the pyrochlore structure. The bigger cations, Ca²⁺, Sr²⁺, Gd³⁺, and Eu³⁺ occupy the A sites at 16d (1/2, 1/2, 1/2) and the B ones, Sn⁴⁺ and Nb⁵⁺ are at 16c sites (0, 0, 0). There are two crystallographically nonequivalent sites for oxygen: one at the 48f sites (x, 1/8, 1/8) and the other at the 8b sites (3/8, 3/8, 3/8). First, the scale factors, zero correction, and background parameters were refined, the cell parameter, 48f oxygen positional parameter (x), full width half-maximum (fwhm) parameters, and isotropic displacement factors being refined next. An asymmetry correction was also applied. The profile was fitted using a pseudo-Voigt profile function. Raman spectra were recorded using a HR800 LabRAM confocal Raman spectrometer operating at 20 mW laser power equipped with a peltier cooled CCD detector. Samples were excited using a He–Ne laser source having an excitation wavelength of 632.8 nm and with an acquisition time of 5 s using a 50× microscope objective. All the spectra are presented after baseline correction. The photoluminescence spectra of the prepared samples were obtained using a Spex-Fluorolog DM3000F spectrofluorimeter with a 450W xenon flash lamp as the exciting source. The excitation and emission slit widths were fixed at 0.5 and 1 nm, respectively, and a filter of 550 nm was used for taking the excitation spectra of samples. The microchemical analysis was performed on an energy dispersive spectrometer (EDS, OXFORD instruments, UK) coupled with an environmental scanning electron microscope (ESEM, FET-Quanta, FEI Netherlands). The selected-area electron diffraction (SAED) patterns and high-resolution electron microscopy of the samples were taken using a TECNAI 30G² S-TWIN transmission electron microscope (FEI, The Netherlands) operating at 300 kV. A small amount of finely powdered sample is dispersed in an acetone medium by ultrasonication, drop-casted onto carbon-coated copper

grids using micropipet, and dried. All measurements were carried out at room temperature.

3. RESULTS AND DISCUSSION

3.1. Red Emitting $\text{CaGd}_{1-x}\text{SnNbO}_7:x\text{Eu}^{3+}$ Phosphors.

Powder XRD patterns of Eu^{3+} -doped $\text{CaGd}_{1-x}\text{SnNbO}_7$ samples shown in Figure 1 exhibit the characteristic pyrochlore peaks.

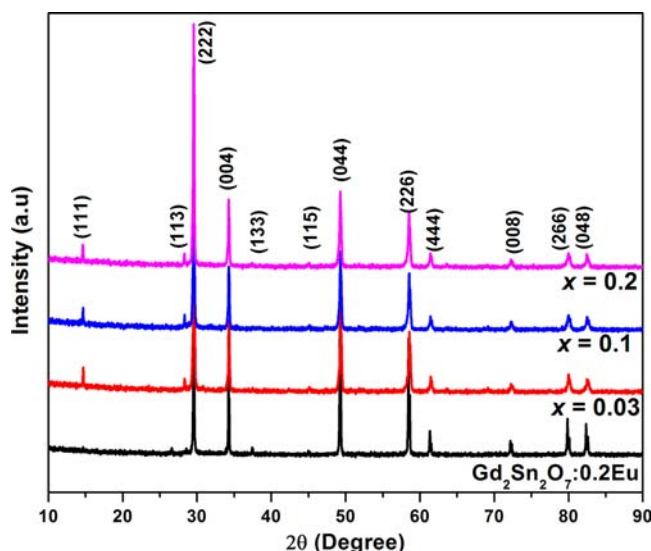


Figure 1. Powder XRD patterns of $\text{CaGd}_{1-x}\text{SnNbO}_7:x\text{Eu}^{3+}$ ($x = 0.03, 0.10,$ and 0.20) calcined at $1300\text{ }^\circ\text{C}$ (6 h) and $\text{Gd}_2\text{Sn}_2\text{O}_7:0.2\text{Eu}^{3+}$. All the peaks can be well assigned to a cubic pyrochlore type structure with a space group $Fd\bar{3}m$. Eu^{3+} doping does not change the phase purity since there are no additional peaks with increase of Eu^{3+} doping concentration. $\text{CaGd}_{1-x}\text{SnNbO}_7:x\text{Eu}^{3+}$ phosphors have intense (111) pyrochlore superlattice peaks in comparison with $\text{Gd}_2\text{Sn}_2\text{O}_7:0.2\text{Eu}^{3+}$.

As the ionic radius and valency of Gd matches with that of Eu effective doping is possible. Absence of impurity peaks along with a small blue shift of (222) peak confirms this. Further, an interesting observation was the increased intensity of characteristic superstructure peaks in CaGdSnNbO_7 in comparison with $\text{Gd}_2\text{Sn}_2\text{O}_7$. Such variation in the intensities of superstructure peaks is associated with the variation in the oxygen position parameter. The elemental analysis using EDS (see Figure S1 in the Supporting Information) confirms the presence of expected elements and the obtained chemical compositions were close to the theoretical stoichiometry.

The excitation spectra of $\text{CaGd}_{1-x}\text{SnNbO}_7:x\text{Eu}^{3+}$ ($x = 0.03, 0.05, 0.10, 0.15,$ and 0.20) shown in Figure 2 has a broad charge transfer (CT) band from 260 to 360 nm centered at 306 nm. This broad CT band is due to the merged effect of $\text{O}_{2p} \rightarrow \text{Eu}_{4f}$ and $\text{O}_{2p} \rightarrow \text{Nb}_{4d}$ charge transfer transitions. The CTB of Eu^{3+} generally lies in the range 250–300 nm and the energy for this process depends on the covalency of the Eu–O bond and the coordination environment of Eu^{3+} . NbO_6 groups have a strong absorption in the 250–310 nm regions (see Figure S2 in the Supporting Information). It can be assumed that the observed CTB in the present excitation spectra corresponds to the CT transitions from O^{2-} to Eu^{3+} and O^{2-} to Nb^{5+} . In complex hosts, the contributions from more than one component in the CTB cannot be resolved due to spectral overlap.^{1,26} For $\text{Gd}_2\text{Sn}_2\text{O}_7:\text{Eu}^{3+}$, the CT band locates at higher energy around 276 nm.^{20,27} As CT band energy depends on the electro-negativity difference between ligand and metal,⁷ substitution of

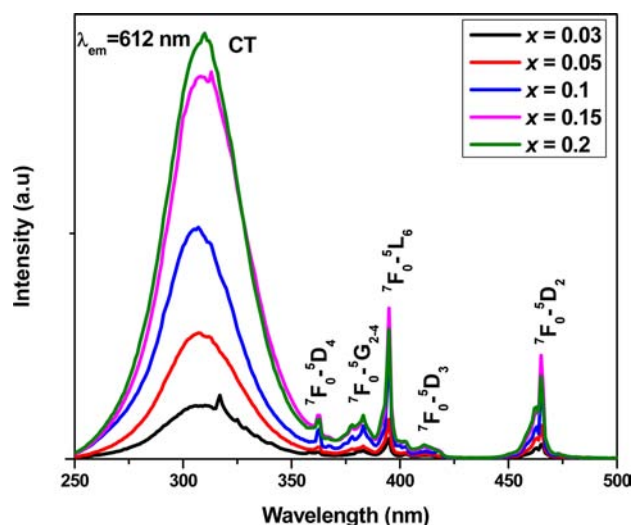


Figure 2. Excitation spectra ($\lambda_{\text{em}} = 612\text{ nm}$) of $\text{CaGd}_{1-x}\text{SnNbO}_7:x\text{Eu}^{3+}$ ($x = 0.03, 0.05, 0.10, 0.15$ and 0.20). The broad band from 260 to 360 nm corresponds to metal–oxygen charge transfer. The sharp peaks beyond 360 nm arise from intraconfigurational $f-f$ transitions of Eu^{3+} . The $f-f$ transition peaks are less intense compared to the broad charge transfer band and are saturated for 15 mol % doping.

less electronegative Ca and Nb ions compared to Gd and Sn to the crystal lattice can result in CT band shifting to lower energy. Other sharp peaks in the excitation spectra correspond to characteristic $f-f$ transition peaks.⁹ Of these, the peaks at 395 and 465 nm are of particular interest as these correspond to emission wavelengths of near UV and blue light LEDs.

Figure 3 shows the emission spectra of $\text{CaGd}_{1-x}\text{SnNbO}_7:x\text{Eu}^{3+}$ ($x = 0.03, 0.05, 0.10, 0.15,$ and 0.20) under 395 nm excitation. In the emission spectra, the hypersensitive ${}^5\text{D}_0\text{-}{}^7\text{F}_2$ ED transition around 612 nm dominates over the MD transition. Hypersensitivity depends on site symmetry of lanthanide ion and the position of charge transfer band.²⁸ Here, Eu^{3+} ions replace Gd^{3+} ions in the A-site which is

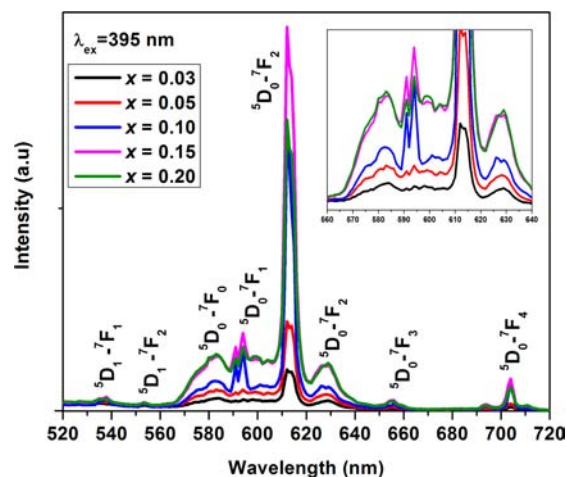


Figure 3. Emission spectra of $\text{CaGd}_{1-x}\text{SnNbO}_7:x\text{Eu}^{3+}$ ($x = 0.03, 0.05, 0.10, 0.15,$ and 0.20) under 395 nm excitation. As ${}^5\text{D}_0\text{-}{}^7\text{F}_2$ electric dipole transition intensity dominates over magnetic dipole transition, Eu^{3+} sites have no inversion symmetry. After 15 mol % doping concentration quenching occurs. The inset shows the enlarged view of MD transitions. For low Eu^{3+} doping splitting of ${}^5\text{D}_0\text{-}{}^7\text{F}_1$, magnetic dipole transition is not observable.

expected to have inversion symmetry. In the present pyrochlore phase the larger cations Ca^{2+} (1.12 Å, CN8), Gd^{3+} (1.05 Å, CN8) and Eu^{3+} (1.07 Å, CN8) occupy the A sites and the smaller Nb^{5+} (0.64 Å, CN6) and Sn^{4+} (0.69 Å, CN6) cations occupy the B sites of the lattice. The probability of nearest neighbor for Eu^{3+} with one type of cation and two types of cations can be predicted like this: $\text{Ca}^{2+}\text{-O}^{2-}\text{-Eu}^{3+}\text{-O}^{2-}\text{-Ca}^{2+}$; $\text{Gd}^{3+}\text{-O}^{2-}\text{-Eu}^{3+}\text{-O}^{2-}\text{-Gd}^{3+}$; and $\text{Ca}^{2+}\text{-O}^{2-}\text{-Eu}^{3+}\text{-O}^{2-}\text{-Gd}^{3+}$; $\text{Gd}^{3+}\text{-O}^{2-}\text{-Eu}^{3+}\text{-O}^{2-}\text{-Ca}^{2+}$; $\text{Ca}^{2+}\text{-O}^{2-}\text{-Gd}^{3+}\text{-O}^{2-}\text{-Eu}^{3+}$; etc. The environment prevails for Eu^{3+} to the nearest neighbor changes with Ca^{2+} and Gd^{3+} either alternatively or one of the two cations, repetitively. With this kind of occupancy of three types of cations shared in the same lattice site, Eu^{3+} loses its site symmetry, thereby enhancing the hypersensitive transitions, ${}^5\text{D}_0\text{-}{}^7\text{F}_0$, ${}^5\text{D}_0\text{-}{}^7\text{F}_2$, and ${}^5\text{D}_1\text{-}{}^7\text{F}_1$. Usually, the site-to-site variation in the local structure around Eu^{3+} will result in broadening of ${}^5\text{D}_0\text{-}{}^7\text{F}_0$ transition. The broadening of the ${}^5\text{D}_0\text{-}{}^7\text{F}_0$ transition in the emission spectra of $\text{CaGd}_{1-x}\text{SnNbO}_7\text{:}x\text{Eu}^{3+}$ directly proves the presence of Eu^{3+} luminescent centers having various local environments. Similar observations are made in $\text{Sr}_{2-x}\text{CeO}_4\text{:}x\text{Ln}^{3+}$ ($\text{Ln} = \text{Eu}, \text{Sm}, \text{Yb}$) phosphors.²⁹ In the case of Eu^{3+} phosphors mixing of $4f^6$ configuration with the levels of opposite parity of the charge transfer state has high probability because the $4f^25d$ state is at very high energy.⁷ So in Eu^{3+} -doped compounds, the energy of charge transfer states can influence the luminescence properties.³⁰ This type of effect is more visible when these compounds are excited under CT band excitation itself as intense ${}^5\text{D}_0\text{-}{}^7\text{F}_0$ bands. Figure S3 in the Supporting Information shows the emission spectra $\text{CaGd}_{0.8}\text{SnNbO}_7\text{:}0.2\text{Eu}^{3+}$ under 306 nm excitations. As the CT band energy is low, the ${}^5\text{D}_0\text{-}{}^7\text{F}_0$ transition can borrow intensity from the ${}^5\text{D}_0\text{-}{}^7\text{F}_2$ transitions.³¹ In the present $\text{CaGd}_{1-x}\text{SnNbO}_7\text{:}x\text{Eu}^{3+}$ phosphors, the distortion of the A site symmetry and red shift of charge transfer energy leads to intense ${}^5\text{D}_0\text{-}{}^7\text{F}_2$ hypersensitive ED transitions under 395 nm excitation.

In pyrochlore phosphors, the ${}^5\text{D}_0\text{-}{}^7\text{F}_1$ MD transition is expected to split into two. One corresponds to the $A_{1g}\text{-}A_{2g}$ transition allowed in the z -direction (corresponds to $[111]$ crystallographic direction) and the other $A_{1g}\text{-}E_g$ transition is allowed along both the x and y directions.⁴ Because the latter is allowed along two directions, in the emission spectra of pyrochlore phosphors one of the split ${}^5\text{D}_0\text{-}{}^7\text{F}_1$ band has double the intensity than the other and the intense band is usually located in the shorter wavelength.^{3,5,32-34} In $\text{CaGd}_{1-x}\text{SnNbO}_7\text{:}x\text{Eu}^{3+}$ phosphors, the ${}^5\text{D}_0\text{-}{}^7\text{F}_1$ MD transition splits into two for $x \geq 0.1$ with almost comparable intensity and the intense peak is located in the higher wavelength region. It clearly indicates the deviation of pyrochlore A-site symmetry from a perfect inversion center and also the distortion of the scalenohedra. Changes in the (111) super lattice peaks of $\text{CaGd}_{1-x}\text{SnNbO}_7\text{:}x\text{Eu}^{3+}$ in comparison with $\text{Gd}_{2-x}\text{Sn}_2\text{O}_7\text{:}x\text{Eu}^{3+}$ are clearly observable in the XRD patterns shown in Figure 1. The increase of (111) superlattice peak intensity is due to the decrease in O_{48f} positional parameter “ x ”. As the “ x ” value decreases, A site scalenohedra becomes more distorted. ${}^5\text{D}_0\text{-}{}^7\text{F}_1$ MD transition splitting is observable for $x \geq 0.1$. It may be an indication of ordering in the pyrochlore structure. The highly intense superlattice peaks in XRD patterns suggests long-range ordering in crystal structure. Sometimes the cation substitution can cause cation/anion ordering in pyrochlore lattice. As XRD is less sensitive to anion ordering, Raman spectrum can be used as a complementary analytical tool that can give additional

information on local ordering, distortion of site symmetry, etc. Raman spectroscopy is very useful in identifying vibration modes (phonons) in solids. The ideal cubic pyrochlore structure belongs to $Fd\bar{3}m$ (O_h^h) space group. The site symmetry is D_{3d} for A and B ions, C_{2v} for the O ions, and T_d for the O' ion. According to group theoretical analysis, the 26 zone center vibrational modes possible are³⁵

$$\Gamma = A_{1g} + E_g + 4F_{2g} + 8F_{1u} + 3A_{2u} + 3E_u + 2F_{1g} + 4F_{2u}$$

Here A_{1g} , E_g , and $4F_{2g}$ are Raman active, $8F_{1u}$ is infrared active, and the rest $2F_{1g}$, $3A_{2u}$, $3E_u$, and $4F_{2u}$ are optically inactive. For pyrochlore structure, the Raman modes involve the movement of oxygen ions only while some IR modes involve motion of the A and B ions. For pyrochlore oxides, higher-frequency bands are due to B–O stretching vibrations, midrange bands are due to O–B–O bending modes, and sometimes A–O' stretching modes may appear as lower-frequency vibrations.³⁶ Raman spectra of $\text{CaGd}_{1-x}\text{SnNbO}_7\text{:}x\text{Eu}^{3+}$ samples are shown in Figure 4. The Gaussian fitting of Raman spectra was done (see Figure

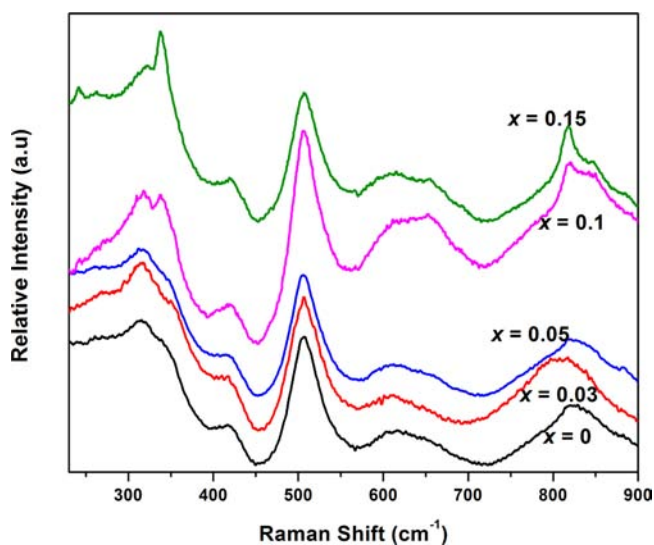


Figure 4. Raman spectra of $\text{CaGd}_{1-x}\text{SnNbO}_7\text{:}x\text{Eu}^{3+}$ phosphors. The ideal cubic pyrochlore structure belongs to $Fd\bar{3}m$ (O_h^h) space group have 6 Raman active modes ($A_{1g} + E_g + 4F_{2g}$). All peaks of $\text{CaGd}_{1-x}\text{SnNbO}_7\text{:}x\text{Eu}^{3+}$ correspond to characteristic pyrochlore vibrational modes. With progressive Eu^{3+} doping the peak around 320 cm^{-1} associated with F_{2g} and E_g bending modes resolves into two separate peaks because of ordering in the crystal lattice. The mode appearing beyond 800 cm^{-1} may be due to the distortion of BO_6 octahedra and subsequent relaxation of the selection rules.

S4 in the Supporting Information) and the resulting vibrational frequencies and tentative assignments of modes are given in Table 1. As Eu doping reaches 10 mol % the broad mode around 320 cm^{-1} resolves into two separate peaks. Long-range-ordered pyrochlore compounds can have short-range disorder because of the presence of vacancy or defects, which leads to broadening of peaks.³⁷ Appearance of narrow peaks in Raman spectra points toward long-range order in the crystal lattice with progressive europium doping. This behavior is in agreement with the photoluminescent studies where the splitting of MD transition peaks is observed for higher europium doping concentrations. Because Eu^{3+} photolumines-

Table 1. Raman Mode Frequencies and Typical Modes of $\text{CaGd}_{1-x}\text{SnNbO}_7:x\text{Eu}^{3+}$ Phosphors

cm^{-1}					typical modes ^{48–51}
$x = 0$	$x = 0.03$	$x = 0.05$	$x = 0.1$	$x = 0.15$	
314	316	313	318	316	E_g mode due to BO_6 bending
349	349	345	343	340	F_{2g} mode due to BO_6 bending
419	418	417	417	419	F_{2g} mode mostly due to B–O stretching with contributions from A–O' stretching and O–B–O bending [*]
508	507	508	505	508	A_{1g} mode due to O–B–O bending
604	600	608	606	607	F_{2g} mode due to B–O stretch

^{*}The one and only mode related to the oxygen ions at the 8b site. All other modes are related to 48f site oxygen anion.⁴⁸ The other high-frequency modes may be due to combination bands or overtones.³⁵

cence spectra is highly sensitive to its local environment, it is effectively used here as a probe to find the short-range disorder within the pyrochlore lattice. Besides Raman spectra analysis, this can be further supported by the variation of asymmetric ratio with europium concentration. The asymmetric ratio (intensity of ${}^5\text{D}_0\text{-}{}^7\text{F}_2$ /intensity of ${}^5\text{D}_0\text{-}{}^7\text{F}_1$) gives some clue on the symmetry of the Eu^{3+} environment. In the present system, the asymmetric ratio increases with the europium concentration (see Figure S5 in the Supporting Information). As always, disorder can give the appearance of higher symmetry, which is true in the present case for low concentrations of Eu^{3+} .^{38,39} The short-range disorder for low concentrations of Eu^{3+} improves the symmetry, which can slightly deviate from D_{3d} symmetry of the structure that lead to no splitting up of the ${}^5\text{D}_0\text{-}{}^7\text{F}_1$ transition.

From the emission spectra shown in Figure 3, with increase in europium doping the intensity of ED transition increases and reaches a maximum for 15 mol % doping after that concentration quenching occurs. As the europium ion concentration increases, the probability for resonance energy transfer between europium ions also increases and this leads to trapping of energy by defects in the crystal and hence in nonradiative energy emission.

3.2. Influence of Sr Substitution on the Optical Properties of $\text{Ca}_{1-y}\text{Sr}_y\text{Gd}_{1-x}\text{SnNbO}_7:x\text{Eu}^{3+}$ Phosphors. As Eu^{3+} emission spectrum can reflect any symmetry or covalent changes within the structure we have used Sr^{2+} as a network modifier ion. Strontium substitution cannot make any significant changes in the crystal structure but of course it will have some influence on the A– O_{8b} chains as it is bigger compared to calcium ions. Figure 5 shows the XRD patterns of Sr-substituted phosphors for 10 mol % Eu^{3+} doping. Solubility limit of Sr ions in place of Ca was found to be 20 mol % after that some impurity peaks are observed. To understand the extent of modification of the lattice with Sr substitution, we carried out Rietveld analysis. Figure 6 shows the typical best fit including observed, calculated, the difference diffraction profiles, and the Bragg positions for $\text{Ca}_{0.8}\text{Sr}_{0.2}\text{Gd}_{0.9}\text{SnNbO}_7:0.1\text{Eu}^{3+}$. Lattice constant, bond distances, and A–A distances of $\text{Ca}_{1-y}\text{Sr}_y\text{Gd}_{1-x}\text{SnNbO}_7:0.1\text{Eu}^{3+}$ phosphors along with R-factors are given in Table 2. The values of R-factors seem to indicate a reliable structure model. As the refinement yielded, strontium is expected to occupy the calcium site based

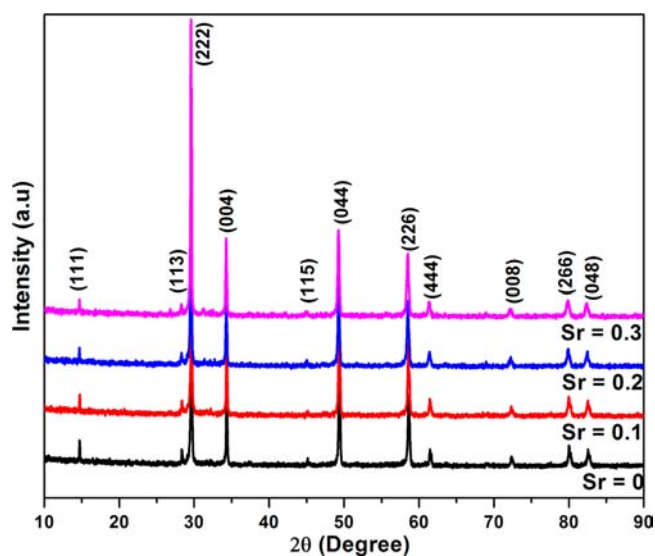


Figure 5. Powder X-ray diffraction patterns of $\text{Ca}_{1-y}\text{Sr}_y\text{Gd}_{0.9}\text{SnNbO}_7:0.1\text{Eu}^{3+}$. For $\text{Sr} = 0.3$, additional impurity peaks appear in the XRD patterns.

on its ionic size and charge neutrality. Lattice parameter and A– O_{8b} bond distance increase with the increase in strontium substitution. The expansion of the crystal lattice with Sr substitution also results in an increased A–A distance.

Accommodating cations having different valency and ionic radii in the pyrochlore A site can cause changes in luminescence properties. From the excitation spectra of $\text{Ca}_{1-y}\text{Sr}_y\text{Gd}_{0.9}\text{SnNbO}_7:0.1\text{Eu}^{3+}$ shown in Figure 7, the intensities of the CT band vary nonuniformly. The enhanced f–f transition intensities are due to increased polarization and distortion in the lattice because of bigger ion substitution.^{40,41} As the Pauling's electronegativities of Ca and Sr are comparable (1 and 0.95), the CT band positions does not show any significant change.

The emission spectra profiles of the Sr substituted phosphors under 395 nm excitation are identical with that of $\text{CaGd}_{1-x}\text{SnNbO}_7:x\text{Eu}^{3+}$, but emission intensities are enhanced with strontium substitution (Figure 8). By keeping Sr substitution at 20 mol % calcium, we varied the Eu^{3+} -doping concentration up to 50 mol %. Electron diffraction pattern from a single particle of $\text{CaGd}_{0.6}\text{SnNbO}_7:0.4\text{Eu}^{3+}$ phosphor shown in Figure 9a is consistent with pyrochlore-type unit cell. The pattern is indexed using the ratio method. From high-resolution TEM images shown in Figure 9b, interplanar spacing is 0.617 nm, which matches with the (111) plane of pyrochlore. The HRTEM and SAED pattern confirm the phase purity of $\text{CaGd}_{0.6}\text{SnNbO}_7:0.4\text{Eu}^{3+}$ phosphor.

$\text{Ca}_{0.8}\text{Sr}_{0.2}\text{Gd}_{1-x}\text{SnNbO}_7: x\text{Eu}^{3+}$ ($x = 0.1, 0.2, 0.3, 0.4$, and 0.5) phosphors show intense red emission and concentration quenching was observed at 40 mol % Eu^{3+} doping (Figure 10). Without Sr substitution we observed quenching at 15 mol % Eu^{3+} doping. With Sr substitution, the pyrochlore lattice constant increases, which can change the optimum Eu concentration, but such a large change in quenching concentration is unexpected.

Eu^{3+} cluster formation can decrease Eu–Eu distance, which in turn will promote resonance energy transfer between excited Eu^{3+} ions and leads to quenching of luminescence. Of course, if such a type of quenching mechanism dominates, it will reflect in the lifetime values also. From decay curves shown in Figure

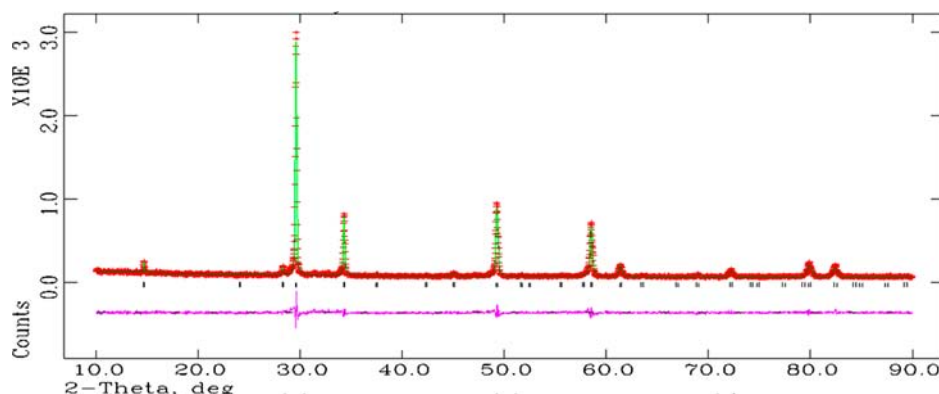


Figure 6. Observed (points), calculated (continuous line), and difference $I_{\text{obsd}} - I_{\text{calcd}}$ (bottom line) profiles obtained after Rietveld refinement of $\text{Ca}_{0.8}\text{Sr}_{0.2}\text{Gd}_{0.9}\text{SnNbO}_7:0.1\text{Eu}^{3+}$ using GSAS program. The powder data was refined using the space group $Fd\bar{3}m$ (No. 227) of pyrochlore structure and the corresponding atomic position set. First, the scale factors, zero correction, and background parameters were refined, with the cell parameter, 48f oxygen positional parameter (x), full width half-maximum (fwhm) parameters, and isotropic displacement factors being refined next. An asymmetry correction was also applied. The profile was fitted using pseudo-Voigt profile function. Vertical bars in the figure indicates the pyrochlore Bragg reflections.

Table 2. Room-Temperature Structural Parameters of $\text{Ca}_{1-y}\text{Sr}_y\text{Gd}_{0.9}\text{SnNbO}_7:0.1\text{Eu}^{3+}$

composition	$y = 0$	$y = 0.1$	$y = 0.2$	$y = 0.3$
lattice constant, a (Å)	10.44628(26)	10.45409(28)	10.46439(32)	10.47144(12)
oxygen x parameter	0.3172(10)	0.3216(9)	0.3203(9)	0.3179(9)
A–O _{48f} (Å)	2.657(7)	2.626(7)	2.638(7)	2.657(7)
A–O _{8b} (Å)	2.26169(4)	2.26338(5)	2.26561(5)	2.26713(2)
B–O _{48f} (Å)	1.975(4)	1.994(4)	1.9907(34)	1.9830(33)
A–A	3.69332(9)	3.69608(10)	3.69972(11)	3.70221(4)
R_p (%)	10.29	10.51	10.29	10.22
R_{vp} (%)	7.97	8.26	8.02	7.82
χ^2 (%)	1.09	1.162	1.089	1.096

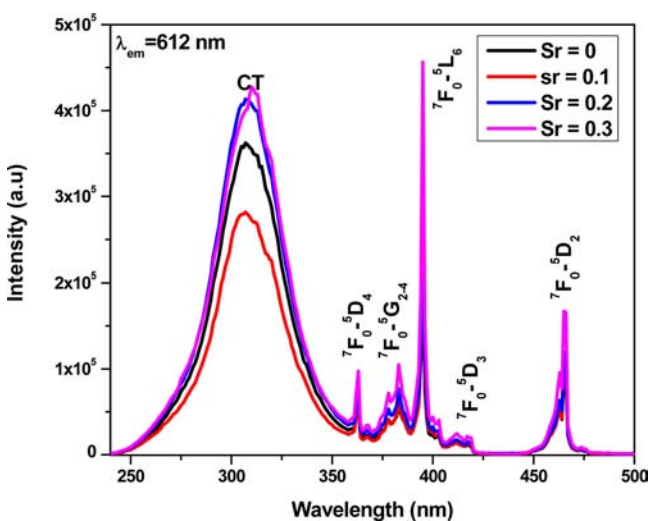


Figure 7. Excitation spectra of $\text{Ca}_{1-y}\text{Sr}_y\text{Gd}_{0.9}\text{SnNbO}_7:0.1\text{Eu}^{3+}$ ($y = 0, 0.1, 0.2,$ and 0.3) monitored for 612 nm emission. With Sr substitution charge transfer band center does not show any significant change but the ${}^7\text{F}_0-{}^5\text{L}_6$ transition dominates over CT band intensity.

11, we obtained the lifetimes of $\text{Ca}_{1-y}\text{Sr}_y\text{Gd}_{0.9}\text{SnNbO}_7:0.1\text{Eu}^{3+}$ ($y = 0, 0.1, 0.2,$ and 0.3) ${}^5\text{D}_0-{}^7\text{F}_2$ red emission as 0.63, 0.61, 0.62, and 0.62 ms, respectively. There is no significant change in the lifetime values with Sr substitution.

Exchange interaction between Eu^{3+} is of great probability for compounds having Eu separation below 5 Å.⁹ As Eu^{3+} doping concentration increases, the rate of exchange energy transfer

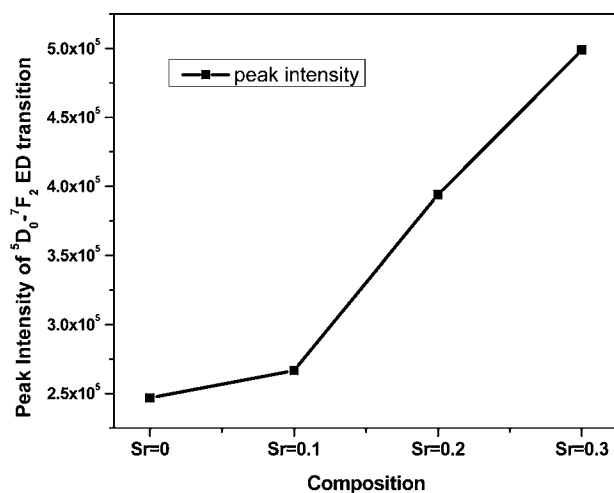


Figure 8. Peak intensities of 612 nm ED transitions of $\text{Ca}_{1-y}\text{Sr}_y\text{Gd}_{0.9}\text{SnNbO}_7:0.1\text{Eu}^{3+}$ ($y = 0, 0.1, 0.2,$ and 0.3) under 395 nm excitation. Intensities get enhanced with progressive Sr substitution.

increases, which leads to the trapping of excitation energy by some killer sites and leads to increased nonradiative transition rates and hence quenching in luminescence. Because no intermediate ladder levels are possible in between the ${}^5\text{D}_0$ and ${}^7\text{F}_j$ levels of Eu^{3+} ion, the above-mentioned energy trapping is the only possible reason for quenching of luminescence. Concentration quenching can be increased if some big anion groups are incorporated into a matrix in which the Eu^{3+} ions do not share any O^{2-} ions.⁴² Pyrochlore structure can be treated as

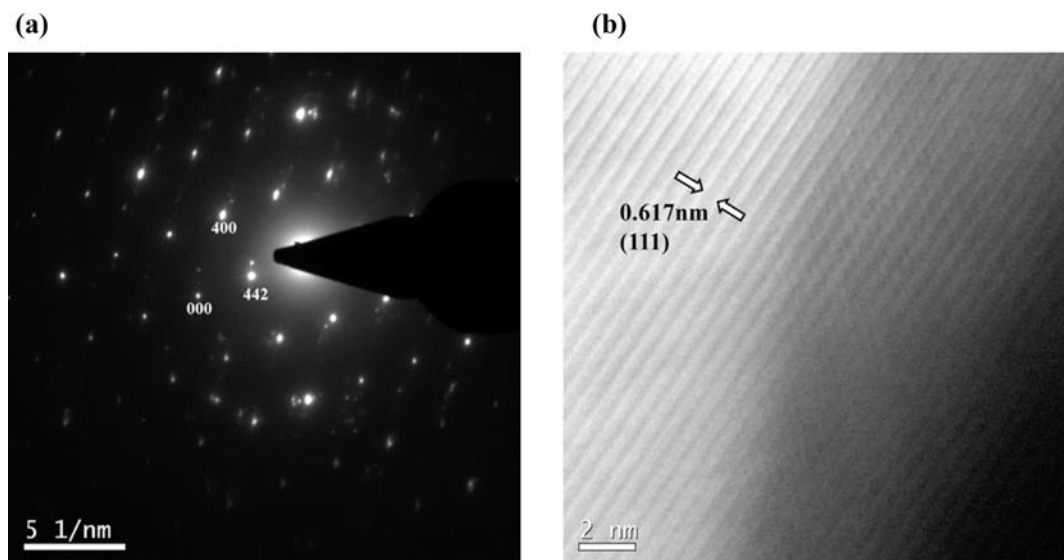


Figure 9. Selected area electron diffraction patterns of (a) $\text{CaGd}_{0.6}\text{SnNbO}_7:0.4\text{Eu}^{3+}$ and (b) its high-resolution TEM image. SAED patterns can be indexed according to the pyrochlore unit cell. The d spacing of HRTEM is matching with the (111) plane.

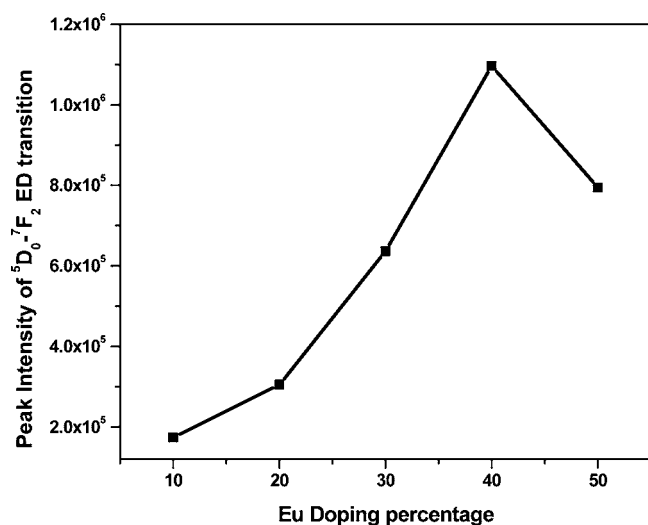


Figure 10. Peak intensities of 612 nm ED transitions of $\text{Ca}_{0.8}\text{Sr}_{0.2}\text{Gd}_{1-x}\text{SnNbO}_7:x\text{Eu}^{3+}$ ($x = 0.1, 0.2, 0.3, 0.4,$ and 0.5) under 395 nm excitation. The phosphors show concentration quenching beyond 40 mol % Eu^{3+} doping.

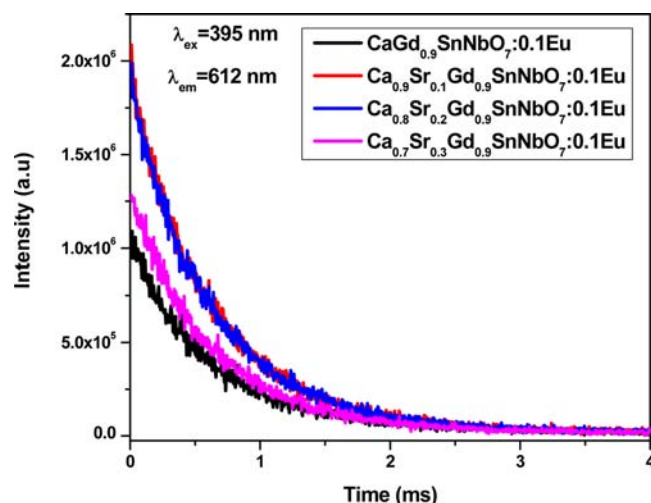


Figure 11. Life time decay curves of ${}^5\text{D}_0\text{-}{}^7\text{F}_2$ transition (wavelength 612 nm) in $\text{Ca}_{1-y}\text{Sr}_y\text{GdSnNbO}_7:0.1\text{Eu}^{3+}$ ($y = 0, 0.1, 0.2,$ and 0.3) under 395 nm excitation. Decay curves can be well fitted with a single exponential decay function $y = Ae^{(-x/t)}$, where “ A ” is a constant and “ t ” is the decay time.

interpenetrating networks of B_2O_6 and $\text{A}_2\text{O}'$ units as shown in Figure 12. The $\text{A-O}'$ linkages form zigzag chains and two such chains intersect at O' . In the present quaternary pyrochlore oxides, there are three types of cations in the A site and we are doping Eu for Gd sites, which decreases the possibility of oxygen ions (O') sharing by Eu^{3+} ions. The incorporation of the big Sr atoms to the lattice can then block resonance energy transfer between Eu^{3+} neighbor ions. The combined effect will be an increased quenching concentration.

3.3. Role of Effective Positive Charge of Eu^{3+} Ions in $\text{Ca}_{0.8-x}\text{Sr}_{0.2}\text{GdSnNbO}_{7+\delta}:x\text{Eu}^{3+}$ Phosphors. The role of effective positive/negative charge of Eu^{3+} ions under CT band excitation are well-investigated and explained using the configurational coordinate model. It is reported that effective positive charge of Eu^{3+} ions will shrink the ground state CT band, which will increase nonradiative crossover between excited and ground-state CT levels and this results in less

efficient phosphor materials.^{43,44} But to the best of our knowledge, role of effective positive charge of Eu^{3+} ions on the luminescence properties under f–f excitation has not been reported. The $\text{Ca}_{0.8-x}\text{Sr}_{0.2}\text{GdSnNbO}_{7+\delta}:x\text{Eu}^{3+}$ offers the possibility of doping Eu^{3+} ions to the Ca site also. The reduction of Ca amount for Eu substitution changes the crystal field but not the lattice site in the $\text{Ca}_{0.8-x}\text{Sr}_{0.2}\text{GdSnNbO}_{7+\delta}:x\text{Eu}^{3+}$.

The XRD patterns of $\text{Ca}_{0.8-x}\text{Sr}_{0.2}\text{GdSnNbO}_{7+\delta}:x\text{Eu}^{3+}$ (Figure 13), show all the pyrochlore characteristic peaks. Above 20 mol % doping, additional impurity peaks were observed in the XRD patterns. The lattice parameter decreases with increase in Eu doping up to 15 mol %, which is evident from the shift of the (222) peak toward the right and after that peak shift toward the left can be observed. As Eu^{3+} replaces Ca^{2+} having higher ionic radii, the lattice value should decrease with the increase in doping. Such anomalies in the XRD pattern may be due to the

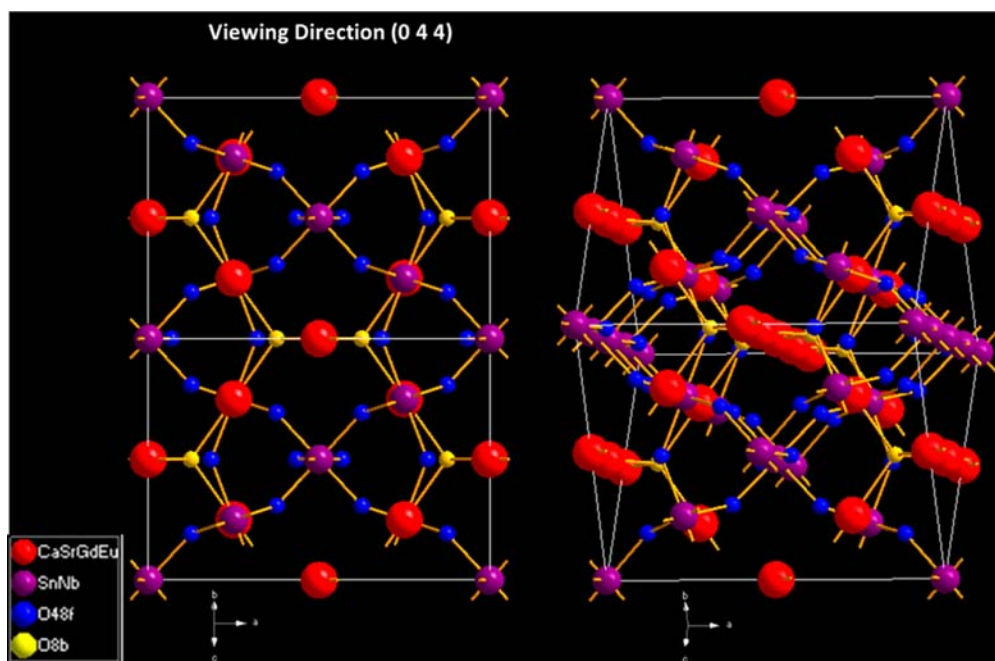


Figure 12. Schematic representation of the pyrochlore unit cell viewed along the (044) direction. The structure contains A_2O' ($O' \rightarrow O_{8b}$) and B_2O_6 ($O \rightarrow O_{48f}$) units. Two A_2O' chains intersect at O' . The A cations also bisect $O_{48f}-B-O_{48f}$ chains.

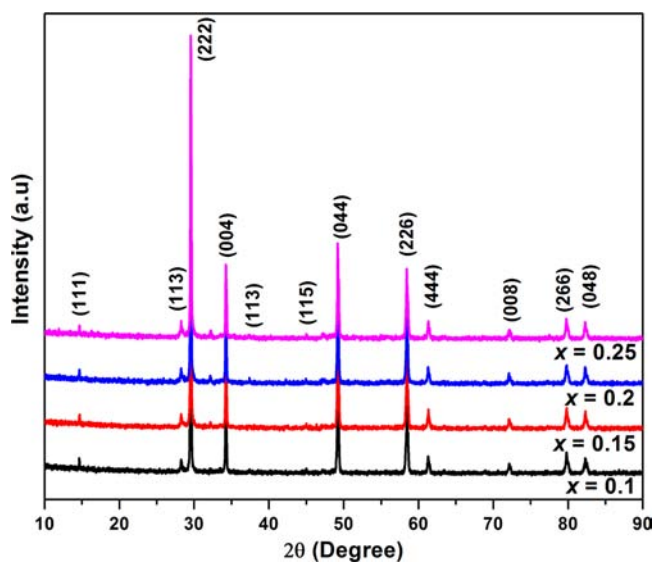


Figure 13. XRD patterns of $Ca_{0.8-x}Sr_{0.2}GdSnNbO_{7+x}Eu^{3+}$ phosphors synthesized at $1400\text{ }^\circ\text{C}$. Here Eu^{3+} is expected to replace Ca^{2+} ions. All diffraction peaks corresponds to characteristic pyrochlore crystal structure. It is clear that in the present pyrochlore phosphors europium activator site exchange is possible without any secondary phase formation.

interstitial oxygen ions in the crystal lattice for maintaining the electrical neutrality of the system. The EDS analysis (see Figure S6 in the Supporting Information) identifies the expected elements and the obtained stoichiometry composition is close to the experimental one.

As powder XRD patterns are less sensitive to small variations in the oxygen occupancy, we have carried out Raman measurements. From Raman spectra, Figure 14, doping of Eu^{3+} ions to the Gd site does not make any significant changes in the relative intensities of Raman modes as both Eu^{3+} and Gd^{3+} ions have comparable ionic radii, electronegativities and

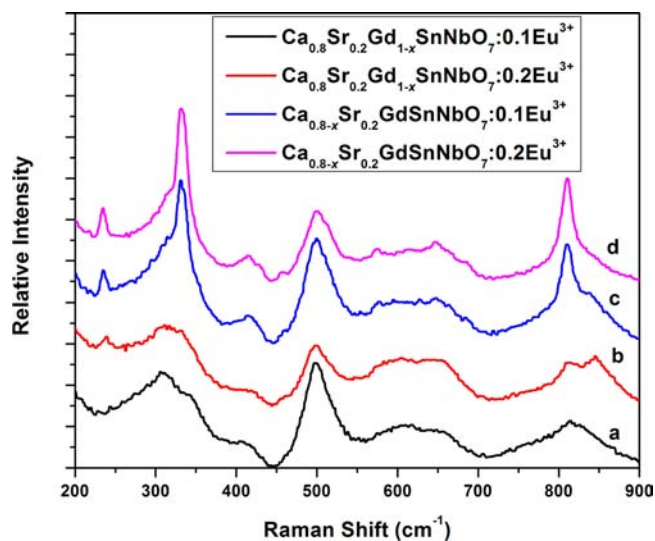


Figure 14. Raman spectra of (a) $Ca_{0.8}Sr_{0.2}Gd_{1-x}SnNbO_7:0.1Eu^{3+}$, (b) $Ca_{0.8}Sr_{0.2}Gd_{1-x}SnNbO_7:0.2Eu^{3+}$, (c) $Ca_{0.8-x}Sr_{0.2}GdSnNbO_7:0.1Eu^{3+}$, and (d) $Ca_{0.8-x}Sr_{0.2}GdSnNbO_7:0.2Eu^{3+}$ phosphors. Relative intensities of A_{1g} ($\sim 500\text{ cm}^{-1}$) and F_{2g} ($\sim 320\text{ cm}^{-1}$) vibrational modes get inverted when Eu^{3+} ions replaces Ca^{2+} ions. fwhm of F_{2g} vibrational modes gets decreased as Eu^{3+} ions replace Ca^{2+} ions in the crystal lattice, which indicates ordering in the pyrochlore lattice.

molecular weights. In $Ca_{0.8}Sr_{0.2}Gd_{1-x}SnNbO_7:xEu^{3+}$ intensities of $O_{48f}-(Sn/Nb)-O_{48f}$ bending A_{1g} ($\sim 500\text{ cm}^{-1}$) vibrational modes are higher than $(Sn/Nb)-O_{48f}(Sn/Nb)$ bending F_{2g} ($\sim 330\text{ cm}^{-1}$) modes. But the intensities of these modes get inverted when Eu^{3+} ions replaces Ca^{2+} ions. From Figure 12, as A cations bisect the $B-O_{48f}-B$ chains in the unit cells, higher electronegative Eu^{3+} ions can pull electrons of O_{48f} ions toward it more strongly than Ca^{2+} ions. This leads to a decrease in the $B-O_{48f}-B$ angle and increases $B-O_{48f}$ bond length.⁴⁵ Such variations lead to changes in intensities of vibrational modes.

Figure 15 shows the excitation and emission spectra of $\text{Ca}_{0.8-x}\text{Sr}_{0.2}\text{GdSnNbO}_{7+\delta}:\text{xEu}^{3+}$ phosphors. One of the remark-

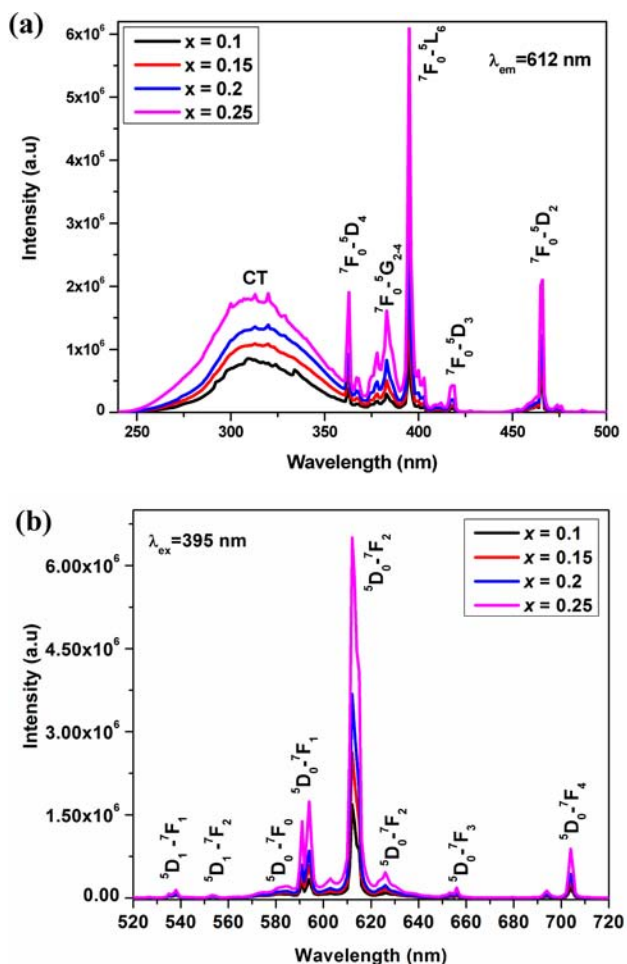


Figure 15. (a) Excitation and (b) emission spectra of $\text{Ca}_{0.8-x}\text{Sr}_{0.2}\text{GdSnNbO}_{7+\delta}:\text{xEu}^{3+}$ phosphors. The excitation spectra show intense ${}^7\text{F}_0\text{-}{}^5\text{L}_6$ transitions. In the emission spectra, intensities of both ${}^5\text{D}_0\text{-}{}^7\text{F}_2$ electric dipole transition and ${}^5\text{D}_0\text{-}{}^7\text{F}_1$ magnetic dipole transition get enhanced. Asymmetric ratio of $\text{Ca}_{0.8-x}\text{Sr}_{0.2}\text{GdSnNbO}_{7+\delta}:\text{xEu}^{3+}$ phosphors are less than that of $\text{Ca}_{0.8}\text{Sr}_{0.2}\text{Gd}_{1-x}\text{SnNbO}_{7+\delta}:\text{xEu}^{3+}$, which suggests that as Eu^{3+} replaces Ca^{2+} ions, the symmetry of A-site of pyrochlore improves. The enhanced intensity is attributed to change of polarization of europium ions as activator site exchanges.

able changes in the excitation spectra is the enhanced f–f transition intensity. Phosphors show excellent red emission intensities and it increased with increase in doping concentration. The enhanced ED transition intensity arises from the symmetry distortion of Eu^{3+} in most cases. The asymmetric

ratio of europium doped $\text{Ca}_{0.8-x}\text{Sr}_{0.2}\text{GdSnNbO}_{7+\delta}:\text{xEu}^{3+}$ phosphors are low compared to $\text{Ca}_{0.8}\text{Sr}_{0.2}\text{Gd}_{1-x}\text{SnNbO}_{7+\delta}:\text{xEu}^{3+}$ as given in Table 3. Incorporation of cations with different valency and electronegativity to the crystal lattice was the reason for distortion of A site of present pyrochlore system. Doping of Eu^{3+} ions to Ca^{2+} sites will decrease the amount of divalent cations in the crystal lattice, which can cause an increase in the lattice symmetry. This is reflected in the emission spectrum where the asymmetric ratio decreased with Eu^{3+} doping.

As both calcium and gadolinium go to the same A site, we do not expect any significant change in emission spectrum. Eu^{3+} in the site of Ca^{2+} ions experiences more positive charge and there will be some red shift in the CT band maxima.²⁴ In the present system, the CT band maxima shows a small red shift to 309 nm from 307 nm as Eu^{3+} goes to Ca^{2+} sites instead of Gd^{3+} sites. However, the change in CTB energy is not significant on substitution of Eu^{3+} in the system, as it is nullified by the decrease in covalency because of reduction in the bond distance (As the incorporation of Eu^{3+} for Ca^{2+} leads to a decrease in bond length based on ionic size consideration²⁴). But the most observable change in the excitation spectra is the increase of (f–f transition peak intensity)/(CT band peak intensity) from 0.78 to 1.68. When Eu^{3+} (ionic radius 1.066 Å, CN8) replaces Ca^{2+} (ionic radius 1.12 Å, CN8) in the crystal lattice, the cationic strength (charge/ionic radius) of the A–O' chains increases. The trivalent europium ions can attract the electron cloud of oxygen ions strongly in comparison with divalent calcium ions. As a result, polarization of europium octahedral will be different in $\text{Ca}_{0.8-x}\text{Sr}_{0.2}\text{GdSnNbO}_{7+\delta}:\text{xEu}^{3+}$ in comparison with $\text{Ca}_{0.8}\text{Sr}_{0.2}\text{Gd}_{1-x}\text{SnNbO}_{7+\delta}:\text{xEu}^{3+}$, and the mixing up of oxygen p orbitals with the f orbitals increases leading to the relaxation of parity selection rule.^{46,47} This contributed for the increased ED transition intensities of $\text{Ca}_{0.8-x}\text{Sr}_{0.2}\text{GdSnNbO}_{7+\delta}:\text{xEu}^{3+}$. A detailed comparison of luminescence properties of all systems are given in Table 3.

4. CONCLUSIONS

A series of new stannate pyrochlore-based red phosphor materials: $\text{CaGd}_{1-x}\text{SnNbO}_7:\text{xEu}^{3+}$, $\text{Ca}_{1-y}\text{Sr}_y\text{Gd}_{1-x}\text{SnNbO}_7:\text{xEu}^{3+}$, and $\text{Ca}_{0.8-x}\text{Sr}_{0.2}\text{GdSnNbO}_{7+\delta}:\text{xEu}^{3+}$ were prepared by the conventional solid state route. Though intense superlattice peaks in the XRD patterns of $\text{CaGd}_{1-x}\text{SnNbO}_7:\text{xEu}^{3+}$ phosphors assign them an ordered pyrochlore structure, the absence of ${}^5\text{D}_0\text{-}{}^7\text{F}_1$ MD splitting for low Eu^{3+} doping is an indication of short-range disorder in the lattice and was further confirmed by Raman analysis. By using Sr as a network modifier ion in place of Ca, though the CT band position does not show any significant change the ${}^7\text{F}_0\text{-}{}^5\text{L}_6$ and ${}^7\text{F}_0\text{-}{}^5\text{D}_2$ transition intensities get enhanced. Substitution of bigger cations to the A site of pyrochlore reduces resonance

Table 3. Excitation and Emission Parameters and Life Times for Different Eu Site Substituted Phosphors

compd	$\text{CaGd}_{0.9}\text{SnNbO}_7:0.1\text{Eu}^{3+}$	$\text{Ca}_{0.8}\text{Sr}_{0.2}\text{Gd}_{0.9}\text{SnNbO}_7:0.1\text{Eu}^{3+}$	$\text{Ca}_{0.7}\text{Sr}_{0.2}\text{GdSnNbO}_{7+\delta}:0.1\text{Eu}^{3+}$
CT band position	307 nm	307 nm	309 nm
peak intensity of CT band	3.6×10^5	4.1×10^5	8.5×10^5
((peak intensity of ${}^7\text{F}_0\text{-}{}^5\text{L}_6$)/(peak intensity of CT band)) ($\lambda_{\text{em}} = 612$ nm)	0.6	0.8	1.7
((intensity of ${}^7\text{F}_2$)/(intensity of ${}^7\text{F}_1$)) ($\lambda_{\text{exc}} = 395$ nm)	5.5	5.4	5
peak intensity of 612 nm red emission ($\lambda_{\text{exc}} = 395$ nm)	2.5×10^5	3.9×10^5	16.8×10^5
lifetimes of ${}^5\text{D}_0\text{-}{}^7\text{F}_2$ emission ($\lambda_{\text{exc}} = 395$ nm)	0.63 ms	0.62 ms	0.64 ms

energy transfer between excited Eu^{3+} ions and leads to an increase in concentration quenching. When europium is doped for the calcium site, the excitation and emission intensities are significantly increased. When europium replaces calcium in the crystal lattice, the mixing of CT band with f orbitals of Eu^{3+} leads to the relaxation of parity selection rule. This contributed for the increased ED transition intensities of $\text{Ca}_{0.8-x}\text{Sr}_{0.2}\text{GdSnNbO}_{7+\delta}:x\text{Eu}^{3+}$. The above results indicate that quaternary pyrochlore system offers a lot of possibilities to manipulate the photoluminescence properties.

■ ASSOCIATED CONTENT

Supporting Information

Additional figures (PDF). This material is available free of charge via the Internet at <http://pubs.acs.org>.

■ AUTHOR INFORMATION

Corresponding Author

*E-mail: padala_rao@yahoo.com. Tel.: + 91 471 2515311. Fax: + 91 471 2491712.

Notes

The authors declare no competing financial interest.

■ ACKNOWLEDGMENTS

S.K.M. acknowledges Council of Scientific and Industrial Research (CSIR), Government of India, for the financial support towards a senior research fellowship.

■ REFERENCES

- (1) Su, Y.; Li, L.; Li, G. *Chem. Mater.* **2008**, *20*, 6060–67.
- (2) Lin, H.-Y.; Fang, Y.-C.; Huang, X.-R.; Chu, S.-Y. *J. Am. Ceram. Soc.* **2010**, *93*, 138–41.
- (3) Hirayama, M.; Sonoyama, N.; Yamada, A.; Kanno, R. *J. Lumin.* **2008**, *128*, 1819–25.
- (4) McCauley, R. A.; Hummel, F. A. *J. Lumin.* **1973**, *6*, 105–15.
- (5) Srivastava, A. M. *Opt. Mater.* **2009**, *31*, 881–85.
- (6) Blasse, G. *Chem. Phys. Lett.* **1973**, *20*, 573–74.
- (7) Blasse, G.; Karl, A. Gschneidner, J. a. L. E. Chemistry and physics of R-activated phosphors. In *Handbook on the Physics and Chemistry of Rare Earths*; Elsevier: Amsterdam, 1979; Vol. 4, Chapter 34, p 237.
- (8) Capobianco, J. A.; Proulx, P. P.; Bettinelli, M.; Negrisolo, F. *Phys. Rev. B* **1990**, *42*, S936–44.
- (9) Blasse, G.; Grabmaier, B. C. *Luminescent Materials*; Springer-Verlag: Berlin, 1994.
- (10) Du, F.; Zhu, R.; Huang, Y.; Tao, Y.; Jin Seo, H. *Dalton Trans.* **2011**, *40*, 11433–40.
- (11) Jüstel, T.; Nikol, H.; Ronda, C. *Angew. Chem., Int. Ed.* **1998**, *37*, 3084–103.
- (12) Ronda, C. R. *Luminescence: from Theory to Applications*; Wiley-VCH: Weinheim, Germany, 2008.
- (13) Subramanian, M. A.; Aravamudan, G.; Subba Rao, G. V. *Prog. Solid State Chem.* **1983**, *15*, 55.
- (14) Nyman, M.; Rodriguez, M. A.; Shea-Rohwer, L. E.; Martin, J. E.; Provencio, P. P. *J. Am. Chem. Soc.* **2009**, *131*, 11652.
- (15) Mahesh, S. K.; Rao, P. P.; Thomas, M.; Radhakrishnan, A. N.; Koshy, P. *J. Mater. Sci.: Mater. Electron.* **2012**, *23*, 1605–09.
- (16) Zhang, Y.; Jia, C.; Su, Z.; Zhang, W. *J. Alloys Compd.* **2009**, *479*, 381.
- (17) Berdowski, P. A. M.; Blasse, G. *J. Solid State Chem.* **1986**, *62*, 317–27.
- (18) Zhu, H.; Yang, D.; Zhu, L.; Li, D.; Chen, P.; Yu, G. *J. Am. Ceram. Soc.* **2007**, *90*, 3095–98.
- (19) Lu, Z.; Wang, J.; Tang, Y.; Li, Y. *J. Solid State Chem.* **2004**, *177*, 3075–79.
- (20) Yang, J. Y.; Su, Y. C.; Chen, Z.; Liu, X. Y. *Adv. Mater. Res.* **2011**, *239–242*, 2851–54.

- (21) Parchur, A. K.; Ningthoujam, R. S.; Rai, S. B.; Okram, G. S.; Singh, R. A.; Tyagi, M.; Gadkari, S. C.; Tewari, R.; Vatsa, R. K. *Dalton Trans.* **2011**, *40*, 7595–601.
- (22) Liu, X.; Han, K.; Gu, M.; Xiao, L.; Ni, C.; Huang, S.; Liu, B. *Solid State Commun.* **2007**, *142*, 680–84.
- (23) Lei, F.; Yan, B. *J. Solid State Chem.* **2008**, *181*, 855–62.
- (24) Hoefdraad, H. E.; Stegers, F. M. A.; Blasse, G. *Chem. Phys. Lett.* **1975**, *32*, 216–17.
- (25) Larson, A. C.; Dreele, R. B. V., *General Structure Analysis System (GSAS)*, Los Alamos National Laboratory Report LAUR 86–748; Los Alamos National Laboratory: Los Alamos, NM, 2004.
- (26) Dutta, P. S.; Khanna, A. *ECS J. Solid State Sci. Technol.* **2013**, *2*, R3153–R67.
- (27) Fu, Z.; Gong, W.; Li, H.; Wu, Q.; Li, W.; Yang, H. K.; Jeong, J. H. *Curr. Appl. Phys.* **2011**, *11*, 933–38.
- (28) Braterman, P.; Blasse, G.; Müller, A.; Baran, E.; Carter, R.; Blasse, G., *The Influence of Charge-Transfer and Rydberg States on the Luminescence Properties of Lanthanides and Actinides Spectra and Chemical Interactions*; Springer: Berlin, 1976; Vol. 26, p 43.
- (29) Nag, A.; Narayanan Kuttly, T. R. *J. Mater. Chem.* **2003**, *13*, 370.
- (30) Blasse, G.; Brill, A. *J. Chem. Phys.* **1966**, *45*, 3327–32.
- (31) Tanaka, M.; Kushida, T. *Phys. Rev. B* **1996**, *53*, 588–93.
- (32) Blasse, G.; Van Keulen, J. *Chem. Phys. Lett.* **1986**, *124*, 534–37.
- (33) Fujihara, S.; Tokumo, K. *Chem. Mater.* **2005**, *17*, 5587–93.
- (34) Li, K.; Li, H.; Zhang, H.; Yu, R.; Wang, H.; Yan, H. *Mater. Res. Bull.* **2006**, *41*, 191–97.
- (35) Arenas, D. J.; Gasparov, L. V.; Qiu, W.; Nino, J. C.; Patterson, C. H.; Tanner, D. B. *Phys. Rev. B: Condens. Matter* **2010**, *82*.
- (36) Henderson, S. J.; Shebanova, O.; Hector, A. L.; McMillan, P. F.; Weller, M. T. *Chem. Mater.* **2007**, *19*, 1712–22.
- (37) Mandal, B. P.; Krishna, P. S. R.; Tyagi, A. K. *J. Solid State Chem.* **2010**, *183*, 41–45.
- (38) Oudet, X. *Ann. Fondation Louis de Broglie* **2012**, *37*, 239–41.
- (39) Oudet, X. *Ann. Chim. Sci. Matér.* **2008**, *33/6*, 435–68.
- (40) Cao, F.-B. *Ind. Eng. Chem. Res.* **2012**, *51*, 3569.
- (41) Cao, F. B.; Tian, Y. W.; Chen, Y. J.; Xiao, L. J.; Wu, Q. *J. Lumin.* **2009**, *129*, 585–88.
- (42) Ju, G.; Hu, Y.; Wu, H.; Yang, Z.; Fu, C.; Mu, Z.; Kang, F. *Opt. Mater.* **2011**, *33*, 1297–301.
- (43) Van Der Voort, D.; Blasse, G. *Chem. Mater.* **1991**, *3*, 1041–45.
- (44) van Ipenburg, M. E.; Dirksen, G. J.; Blasse, G. *Mater. Chem. Phys.* **1995**, *39*, 236–38.
- (45) Zhang, T. T.; Li, K. W.; Zeng, J.; Wang, Y. L.; Song, X. M.; Wang, H. *J. Phys. Chem. Solids* **2008**, *69*, 2845–51.
- (46) Blasse, G., The influence of charge-transfer and rydberg states on the luminescence properties of lanthanides and actinides. In *Spectra and Chemical Interactions*; Springer: Berlin, 1976; Vol. 26, pp 43–79.
- (47) Mishra, K. C.; Berkowitz, J. K.; Johnson, K. H.; Schmidt, P. C. *Phys. Rev. B* **1992**, *45*, 10902–06.
- (48) Sayed, F. N.; Grover, V.; Bhattacharyya, K.; Jain, D.; Arya, A.; Pillai, C. G. S.; Tyagi, A. K. *Inorg. Chem.* **2011**, *50*, 2354–65.
- (49) Qu, Z.; Wan, C.; Pan, W. *Chem. Mater.* **2007**, *19*, 4913–18.
- (50) Babu, G. S.; Valant, M.; Page, K.; Llobet, A.; Kolodiaznyh, T.; Axelsson, A.-K. *Chem. Mater.* **2011**, *23*, 2619–25.
- (51) Ning, P.; Li, L.; Zhang, X.; Wang, M.; Xia, W. *Mater. Lett.* **2012**, *87*, 5.